

This is the accepted manuscript made available via CHORUS. The article has been published as:

## Refined similarity hypothesis using three-dimensional local averages

Kartik P. Iyer, Katepalli R. Sreenivasan, and P. K. Yeung

Phys. Rev. E **92**, 063024 — Published 28 December 2015

DOI: [10.1103/PhysRevE.92.063024](https://doi.org/10.1103/PhysRevE.92.063024)

# Refined similarity hypothesis using 3D local averages

Kartik P. Iyer\*

*Department of Physics and INFN, University of Rome Tor Vergata, Rome, 00133, Italy*

Katepalli R. Sreenivasan

*Departments of Physics and Mechanical Engineering and the Courant Institute of Mathematical Sciences  
New York University, Brooklyn, 11201, USA*

P.K. Yeung

*Schools of Aerospace Engineering and Mechanical Engineering,  
Georgia Institute of Technology, Atlanta, 30332, USA*

(Dated: December 1, 2015)

The refined similarity hypotheses of Kolmogorov, regarded as an important ingredient of intermittent turbulence, has been tested in the past using one-dimensional data and plausible surrogates of energy dissipation. We employ data from direct numerical simulations, at the **microscale** Reynolds number  $R_\lambda \sim 650$ , on a periodic box of  $4096^3$  grid points to test the hypotheses using 3D averages. In particular, we study the small-scale properties of the stochastic variable  $V = \Delta u(r)/(r\epsilon_r)^{1/3}$ , where  $\Delta u(r)$  is the longitudinal velocity increment and  $\epsilon_r$  is the dissipation rate averaged over a three-dimensional volume of linear size  $r$ . **We show that  $V$  is universal in the inertial subrange. In the dissipation range, the statistics of  $V$  are shown to depend solely on a local Reynolds number.**

**PACS numbers:** May be entered using the `\pacs{#1}` command.

## I. INTRODUCTION

A statistical description of the local flow structure in high-Reynolds number turbulence, known as K41, was given in Ref. [1]. In its simplified version, the first hypothesis relates the probability density function (PDF) of the longitudinal velocity increments  $\Delta u(r) = [\mathbf{u}(\mathbf{x} + \mathbf{r}) - \mathbf{u}(\mathbf{x})] \cdot \mathbf{r}/|\mathbf{r}|$  to the mean energy dissipation rate  $\langle \epsilon \rangle$  and the fluid viscosity ( $\nu$ ), for spatial separations  $r = |\mathbf{r}| \ll L$ ,  $L$  being the integral scale of the turbulence. The second hypothesis is that if the Reynolds number is very large, there exists a range of scales (the so-called inertial range) for which  $\nu$  becomes irrelevant, so that the PDF of  $\Delta u(r)$  depends only on  $\langle \epsilon \rangle$ , apart from  $r$  itself. An exact result for the third moment of  $\Delta u(r)$  in the inertial range is given in Ref. [2] as

$$\langle (\Delta u(r))^3 \rangle = -\frac{4}{5} \langle \epsilon \rangle r. \quad (1)$$

An implicit assumption in K41 is that the rate of transfer of energy from the large to the small scales is a constant (or mildly varying) everywhere in the flow and is equal to (or not far from)  $\langle \epsilon \rangle$ . However, the energy dissipation rate per unit mass of a turbulent fluid, given by

$$\epsilon(\mathbf{x}, t) = \frac{\nu}{2} \sum_{i,j} \left( \frac{\partial u_i}{\partial x_j} + \frac{\partial u_j}{\partial x_i} \right)^2, \quad (2)$$

fluctuates wildly in space and time[3]. The fluctuations of  $\epsilon(\mathbf{x}, t)$  may depend on the Reynolds number and

the large-scale properties, which can be non-universal. (Refs. [4–6]).

The refined similarity theory (Ref. [7]), also known as K62, introduced more restrictive alternatives and abandoned strict universality. It postulated that one of the most important factors determining the statistics of  $\Delta u(r)$  for  $r \ll L$  is the dissipation rate averaged over a local volume  $\mathcal{V}(r)$  of linear dimension  $r$ , i.e., the quantity (Ref. [8])

$$\epsilon_r(\mathbf{x}, t) = \frac{1}{r^3} \int_{\mathcal{V}(r)} \epsilon(\mathbf{x} + \mathbf{r}', t) d\mathbf{r}'. \quad (3)$$

Following Ref. [7], the quantities  $r$  and  $\epsilon_r(\mathbf{x}, t)$  can be used to construct a velocity scale at the point  $(\mathbf{x}, t)$  as  $U_r = (r\epsilon_r)^{1/3}$ , and a local Reynolds number can be formed as

$$Re_r = \frac{U_r r}{\nu} = \frac{(r\epsilon_r)^{1/3} r}{\nu} = \left( \frac{r}{\eta_r} \right)^{4/3}, \quad \eta_r = \left( \frac{\nu^3}{\epsilon_r} \right)^{1/4}, \quad (4)$$

where  $\eta_r$  is the local Kolmogorov length scale. The first refined similarity hypothesis can be stated (Ref. [9]), for  $r \ll L$ , as

$$\Delta u(r) \equiv V(r\epsilon_r)^{1/3}, \quad (5)$$

where  $V$  is a **dimensionless** stochastic variable whose PDF depends only on  $Re_r$ . The second refined hypothesis states that if  $Re_r \gg 1$ , the PDF of  $V$  becomes independent of  $Re_r$ , i.e., it is universal.

The first and the second hypotheses relate the scaling exponents of the local dissipation to that of the velocity increments [5]. In particular, the exponent  $\zeta_p$  of velocity increments is related to the exponent  $\tau_p$  of the local

---

\* kartik.iyer@roma2.infn.it

dissipation for the moment of order  $p$  as

$$\zeta_p = \frac{p}{3} + \tau_{p/3}. \quad (6)$$

By independently measuring the scaling exponents of velocity and local dissipation at the small scales, Eq. 6 can be used to verify the K62 hypotheses [10]. However, such an analysis of Eq. 5, can obscure the importance of the stochastic function  $V$ . For instance, the third moment of  $V$  is linked to the mechanism of vortex stretching and energy transfer between different scales [9]. Moreover, although  $V$  is the ratio of two intermittent quantities, it is itself not intermittent [9] and is less sensitive to finite sampling effects.

Previous work (Refs. [9],[11]) have examined the two refined similarity hypotheses using one-dimensional (1D) averages of the local dissipation rate  $\hat{\epsilon}_r(\mathbf{x}, t)$ , calculated over a line  $\mathcal{L}$  of length  $r$  as,

$$\hat{\epsilon}_r(\mathbf{x}, t) = \frac{1}{r} \int_{\mathcal{L}} \epsilon(\mathbf{x} + \mathbf{r}', t) dr'. \quad (7)$$

The use of 1D averages over 3D averages in experiments is partly forced by difficulties in obtaining well-resolved measurements in 3D at high-Reynolds-numbers, especially for small spatial separations  $r \ll L$ . Computationally, 1D averages are easier to calculate than 3D averages, since the latter may require heavy communication between different processors in a parallel network, especially when the spatial separation  $r$  is large.

In this paper, we examine the first and the second postulates of the refined similarity theory using 3D local averages of dissipation. A brief overview of the numerical procedure is given in section II. Some properties of 3D averaged dissipation are juxtaposed with those of 1D averaged dissipation in section III. Results for the K62 theory are presented for a 4096<sup>3</sup> simulation at  $R_\lambda \sim 650$  in section IV. We summarize the main results in section V.

## II. NUMERICAL PROCEDURE

### A. Direct Numerical Simulations

The fluctuating velocity field  $\mathbf{u}(\mathbf{x}, t)$  obeys the forced Navier-Stokes equations for an incompressible flow as

$$\nabla \cdot \mathbf{u} = 0, \quad (8)$$

$$\partial \mathbf{u} / \partial t + \mathbf{u} \cdot \nabla \mathbf{u} = -\nabla p / \rho + \nu \nabla^2 \mathbf{u} + \mathbf{f}, \quad (9)$$

where,  $\rho$  is the constant fluid density and  $\mathbf{f}$  is the random forcing used to achieve stationarity [12]. The domain is a periodic cube with edge length  $2\pi$  with  $N$  grid points to a side. A Fourier pseudospectral method is used for spatial discretization and the equations are integrated in time using a second order Runge-Kutta scheme as given in Ref. [13]. Aliasing errors from the nonlinear term are effectively controlled by removing all coefficients with wave-number magnitude greater than  $k_{max} = (\sqrt{2}/3)N$ .

The non-dimensional parameter  $k_{max}\eta$  gives the resolution of the simulation. The ratio of the grid spacing ( $\Delta x = 2\pi/N$ ) to the Kolmogorov length scale ( $\eta$ ) is,  $\Delta x/\eta \approx 2.96/(k_{max}\eta)$ . Parameters of interest for the simulations used in this work are summarized in Table I. Details about the parallel implementation are given in Ref. [14].

### B. Local 3D averages

Samples of the 1D and 3D local averages of dissipation, ( $\hat{\epsilon}_r, \epsilon_r$ ) are calculated at the point  $(x_1, y_1, z_1)$  over a cube with edge length of  $r$  grid spacing using the formulae,

$$\hat{\epsilon}_r(x_1, y_1, z_1) = \frac{1}{(r+1)} \sum_{x=x_1}^{x_{r+1}} \epsilon(x, y_1, z_1), \quad (10)$$

$$\epsilon_r(x_1, y_1, z_1) = \frac{1}{(r+1)^3} \sum_{z=z_1}^{z_{r+1}} \sum_{y=y_1}^{y_{r+1}} \sum_{x=x_1}^{x_{r+1}} \epsilon(x, y, z). \quad (11)$$

In order to obtain adequately converged statistics of  $\hat{\epsilon}_r$  and  $\epsilon_r$ , Eqs. 10 and 11 need to be used at every point  $(x, y, z)$  in a  $N^3$  grid. The 1D averages are computed along the three orthogonal directions for adequate sampling. The examination of the statistics of  $\hat{\epsilon}_r$  and  $\epsilon_r$  at various scale sizes, requires Eqs. 10 and 11 to be used at all non-trivial spatial separations, which spans  $r = 1, 2, \dots, N/2$  grid spacings. To save computer time, the calculations are performed only at selected multiples of grid spacing, at the larger spatial separations. In the case of 3D local averages, added to the computational complexity, is the inter-processor communication time due to the domain decomposition in a parallel algorithm. The significant computation and communication costs involved, makes the calculation of 3D local averages very challenging, especially at higher Reynolds numbers. Details of the parallel algorithm we used to compute the 3D local averages can be found in Ref. [15].

### C. Calculation of stochastic variable $V$

Consider the stochastic variable  $V$  (Eq. 5) defined as

$$V(r) = \Delta u(r)/(r\epsilon_r)^{1/3}, \quad (12)$$

TABLE I. Summary of the microscale Reynolds number ( $R_\lambda$ ), number of grid points ( $N^3$ ) and resolution ( $k_{max}\eta$ ) for the periodic cube with edge length  $2\pi$  studied in this work.

$R_\lambda$	$N^3$	$k_{max}\eta$
240	512 <sup>3</sup>	1.4
240	2048 <sup>3</sup>	5.7
650	4096 <sup>3</sup>	2.7

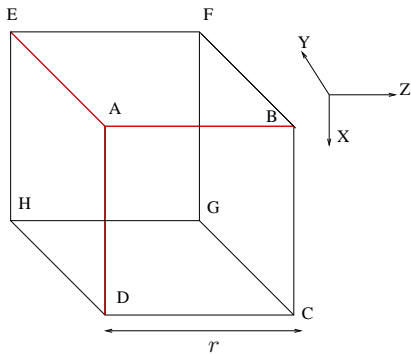


FIG. 1. (Color online) Cube of edge length  $r$  used for the calculation of  $V(r)$ . Line segments AD, AE and AB denote edges along which  $V$  (Eq. 13) is calculated in the  $X$ ,  $Y$  and  $Z$  directions respectively.

where  $\Delta u(r) = [\mathbf{u}(\mathbf{x} + \mathbf{r}) - \mathbf{u}(\mathbf{x})] \cdot \mathbf{r}/|\mathbf{r}|$  is the longitudinal velocity increment along separation vector  $\mathbf{r}$ , whose magnitude is  $r = |\mathbf{r}|$  and  $\epsilon_r$  is the 3D local average of dissipation.

It may be noted here that the probability distribution of  $V$  can be regarded as a ratio distribution since  $V$  is the ratio of random variables (Eq. 12). At scales  $r \ll L$ , both the velocity increments and the local dissipation  $\epsilon_r$  are intermittent and essentially non-Gaussian. All non-negative moments of  $V(r)$  for  $r \ll L$  are well-defined and finite. In particular,  $V$  is not a Cauchy variable [16] at least at the small scales ( $r \ll L$ ).

Since a cube such as that in Fig. 1 has twelve edges over which a longitudinal velocity increments can be defined, we can have twelve different samples of  $V$ . Presumably in isotropic homogeneous turbulence the statistics of  $V$  along these twelve directions can be considered as different samples which can then be averaged. In this work we consider samples of  $V(r)$  along three edges of a cube of length  $r$  as

$$V_\alpha(r) = \frac{\Delta u_\alpha(r)}{(r\epsilon_r)^{1/3}}, \quad \alpha = 1, 2, 3. \quad (13)$$

Here,  $\Delta u_\alpha(r)$  for  $\alpha = 1, 2, 3$  correspond to the longitudinal velocity increments along edges AD, AE and AB respectively in Fig. 1. The samples  $V_\alpha$  for  $\alpha = 1, 2, 3$  can be considered as different realizations for the statistics of  $V$  and can be averaged accordingly. The use of three different samples of  $V$  in this manner improves the statistical stability, especially when the averaging length  $r$  is small ( $r \sim \eta$ ).

### III. RESULTS

#### A. Local averages of dissipation

Figure 2 shows the second moments of local 3D and 1D averaged dissipation as a function of spatial separation for two different resolutions at a given Reynolds num-

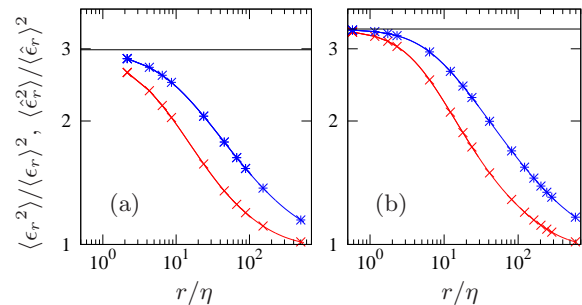


FIG. 2. (Color online) Second order moments of 3D local averages ( $\times$ ) and 1D local averages ( $*$ ) of dissipation for (a)  $k_{max}\eta = 1.4$ , (b)  $k_{max}\eta = 5.7$ , both at  $R_\lambda \sim 240$ . Horizontal solid lines correspond to second order dissipation moment ( $\langle \epsilon^2 \rangle / \langle \epsilon \rangle^2$ ).

ber. It is clear that the 3D local average is more resolution limited than the 1D average for smaller separations. Consider local averages over a cube with edge length  $\Delta$ . A sample of the 1D average represents the dissipation at the midpoint of an edge in the cube, whereas the 3D average represents the dissipation at the centroid of the cube, which is  $\sqrt{3}$  times further away from the given grid point than the corresponding 1D average. Hence 1D averages are closer to the point-wise averages than their 3D counterparts and thereby have better spatial resolution.

For a given spatial separation, the second moment of 3D averaged dissipation is smaller than that of 1D averaged dissipation (Fig. 2), indicating that  $\epsilon_r$  may be less intermittent than  $\hat{\epsilon}_r$  (see also [17]). It has been verified (although not shown here) that this is also true for all higher order moments. For a given averaging length  $r$ , we can indeed write

$$\langle \epsilon_r^q \rangle \leq \langle \hat{\epsilon}_r^q \rangle \leq \langle \epsilon^q \rangle, \quad q = 1, 2, 3, \dots, \quad (14)$$

equality occurring when  $q = 1$ .

To compare the likelihood of extreme events of dissipation, we show in Fig. 3 the PDF for the single-point, 3D and 1D averaged dissipation at two different resolutions at the same Reynolds number. The right-tails of the PDF which correspond to large dissipation events get wider with increased resolution. This effect is more pronounced in the 1D averaged dissipation than in the 3D averaged dissipation. In contrast, the left-tails of the PDF correspond to smaller dissipation events and are less-sensitive to resolution, but benefit from increased sampling in the higher resolution case. For a given scale size, the PDF of  $\hat{\epsilon}_r$  has wider tails than that of  $\epsilon_r$ , indicating that the probability of 1D dissipation taking extreme values is greater than that of 3D dissipation. This is consistent both with the trends for the second order moments of dissipation shown in Fig. 2 and relation 14. A reduced variability at a given Reynolds number can potentially render the 3D averaged dissipation less sensitive to finite sampling effects as compared to 1D dissipation.

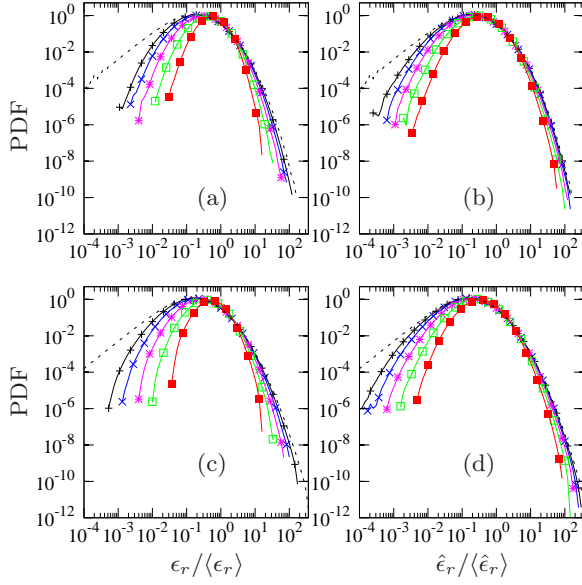


FIG. 3. (Color online) PDF of local 3D dissipation ( $\epsilon_r$ ) and 1D dissipation ( $\hat{\epsilon}_r$ ) at  $R_\lambda \sim 240$  for (a)  $\epsilon_r$ ,  $k_{max}\eta = 1.4$ , (b)  $\hat{\epsilon}_r$ ,  $k_{max}\eta = 1.4$ , (c)  $\epsilon_r$ ,  $k_{max}\eta = 5.7$  and (d)  $\hat{\epsilon}_r$ ,  $k_{max}\eta = 5.7$ . Curves in each frame correspond to scale separations  $r/\eta \approx 2$  (+), 4 (x), 8 (\*), 16 (□) and 32 (■) respectively. Dashed curves correspond to PDF of point-wise dissipation ( $\epsilon/\langle\epsilon\rangle$ ).

### B. Preliminary results

As a prelude to the main results, we provide some basic small-scale information for the  $4096^3$  simulation. Figure 4 shows the compensated energy spectra at  $R_\lambda \sim 650$ . The inertial range constant for the longitudinal 1D spectrum is approximately 0.53 which is consistent with the conclusions of [18]. Figure 5 shows the normalized third-

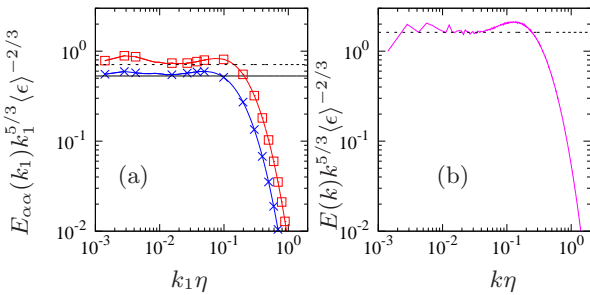


FIG. 4. (Color online) Compensated energy spectra at  $4096^3$ ,  $R_\lambda \sim 650$ . (a) Longitudinal (x) and transverse (□) spectra as functions of wavenumber magnitude in  $k_1$  direction, correspond to  $\alpha = 1, 2$  respectively. Solid horizontal line at  $C_k = 0.53$  is the inertial range constant for longitudinal spectrum from experiments (Ref. [18]). Corresponding constant for the transverse spectrum is given by the dotted line at  $4C_k/3$ . (b) Three-dimensional energy spectrum as a function of wavenumber magnitude  $k$ . Dotted horizontal line at  $55C_k/18$  shows the Kolmogorov constant.

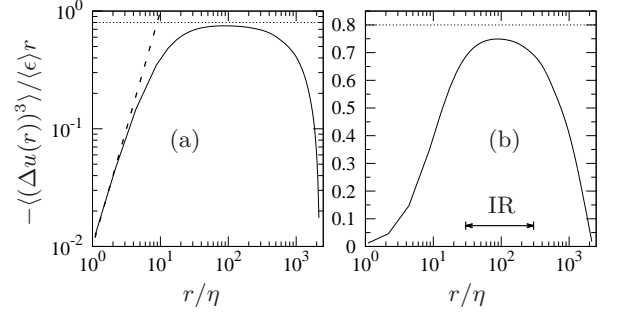


FIG. 5. Normalized third-order velocity structure function at  $4096^3$ ,  $R_\lambda \sim 650$ , averaged over the three Cartesian directions. (a) Log-log scales to check small- $r$  behavior, dashed line corresponds to  $r^2$  to check small- $r$  slope. (b) Log-linear scales to assess inertial range extent. Dotted line at 0.8 for comparison with Eq. 1. The inertial range (IR) is taken as  $30 < r/\eta < 300$ . Ratio of the integral scale to the Kolmogorov scale  $L/\eta \approx 1000$ .

order longitudinal velocity structure function at  $R_\lambda \sim 650$ . The component averaged result (averaged over the three Cartesian directions) shown here, is used to assess the extent of the inertial range. At  $R_\lambda \sim 650$ , the scale separation is wide enough ( $L/\eta \approx 1000$ ) to meaningfully contrast the small scales ( $r \ll L$ ) from the energy-containing large scales. The lack of convergence with the K41 plateau (refer Eq. 1) is at least partly due to the effects of finite sampling and periodic boundary conditions, at the intermediate scales. The effect of limited sampling is more pronounced at higher Reynolds numbers, at which  $\Delta u(r)$  is known to be intermittent in the inertial range [9]. For a given box length, periodic boundary conditions influence the inertial range statistics calculated along the Cartesian directions to a greater extent than those calculated using other directions. Nevertheless, a reasonable estimate for the inertial range for the present simulation from Fig. 5 is  $30\eta < r < 300\eta$ .

Since we are interested in the properties of the stochastic variable  $V$ , it is useful to study the correlation between the velocity increment  $\Delta u(r)$  and the local velocity scale  $(r\epsilon_r)^{1/3}$ . The correlation coefficient between  $\Delta u(r)$  and  $(r\epsilon_r)^{1/3}$  is plotted in Fig. 6. The two quantities are insignificantly correlated at all spatial separations as a consequence of isotropy. The minor deviations at the largest scales may be due to anisotropic effects of forcing and finite domain size considerations. Considering  $|\Delta u(r)|$  instead of  $\Delta u(r)$  results in stronger correlation (Fig. 6) at the small scales. Figure 6 shows that the correlation coefficient between  $|\Delta u(r)|$  and  $(r\epsilon_r)^{1/3}$  varies between 0.15 and 0.35 in the inertial range. These results are consistent with those reported in Ref. [9] and serve as useful checks on the validity of the data.



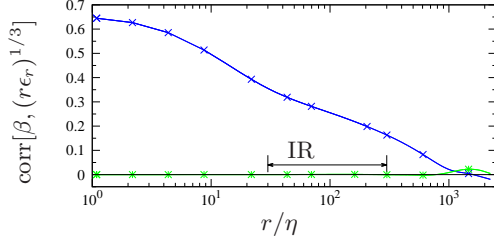


FIG. 6. (Color online) Correlation coefficient as a function of spatial separation between  $(r\epsilon_r)^{1/3}$  and the quantity  $\beta$  where  $\beta$  is  $\Delta u(r)$  (\*) and  $|\Delta u(r)|$  (x) for  $R_\lambda \sim 650, 4096^3$ . Correlation coefficient is defined as  $\text{corr}(x, y) = \langle (x - \langle x \rangle)(y - \langle y \rangle) \rangle / \sigma_x \sigma_y$ , where  $\sigma_x$  and  $\sigma_y$  are the standard deviations of  $x$  and  $y$ . The inertial range (IR) is marked for reference.

### C. K62: the second hypothesis

The second K62 hypothesis is that at sufficiently large local Reynolds number, the PDF of  $V(r)$  for  $\eta \ll r \ll L$  becomes independent of  $Re_r$  and hence is universal. In our simulations, the viscosity is a constant. Hence it suffices to check for the dependence of  $V$  on the local velocity scale  $(r\epsilon_r)^{1/3}$  and the separation length  $r$ .

Figure 7 shows the PDF of  $V$  conditioned on  $(r\epsilon_r)^{1/3}$  for four separation distances. In each frame of Fig. 7, the PDFs marked as A, B and C correspond to the lowest  $Re_r$  and are distinct from the unmarked PDFs which correspond to higher  $Re_r$ , which coalesce, with the shape being preserved in going from one separation distance to another. The collapse of the PDFs of  $V$  at higher  $Re_r$ , indicates an approximate independence of  $V$  from  $\epsilon_r$  and  $r$  in the inertial range. The universality of  $V$  as evidenced by the collapse of the PDFs at high enough  $Re_r$  is more pronounced at the intermediate separations (frames (b) and (c) in Fig. 7), where non-inertial effects such as viscosity and large-scale forcing are less important (Fig. 5).

In order to further test the dependence of  $V$  on  $(r\epsilon_r)^{1/3}$ , we consider the mean value  $|\Delta u(r)|$  conditioned on  $(r\epsilon_r)^{1/3}$ . It follows from Eq. 5 that

$$\langle |\Delta u(r)| | (r\epsilon_r)^{1/3} \rangle = (r\epsilon_r)^{1/3} \langle |V| | (r\epsilon_r)^{1/3} \rangle \quad (15)$$

If  $V$  were independent of  $(r\epsilon_r)^{1/3}$  in the inertial range, it is clear that the left-hand side of Eq. 15 would be a linear function of  $(r\epsilon_r)^{1/3}$  for all values of  $r$  in the inertial range. In such a scenario, Eq. 15 becomes

$$\langle |\Delta u(r)| | (r\epsilon_r)^{1/3} \rangle = (r\epsilon_r)^{1/3} \langle |V| \rangle, \quad \eta \ll r \ll L. \quad (16)$$

Figure 8 shows that this indeed is the case, except possibly at the tails where the sampling uncertainty can be large. This confirms that  $|V|$  as well as  $V$  are independent of  $(r\epsilon_r)^{1/3}$  in the inertial range.

Since  $V$  is approximately independent of  $(r\epsilon_r)^{1/3}$  in the inertial range, it follows that the correlation between  $|V|$  and  $(r\epsilon_r)^{1/3}$  in this scale range should be zero. Figure 9 shows that the correlation coefficient between  $|V|$  and

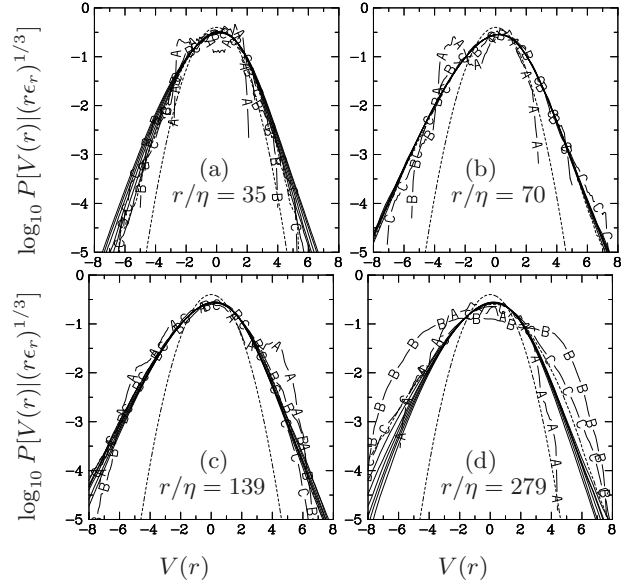


FIG. 7. Conditional PDF of  $V(r)$  for a given spatial separation. The separation distance  $r/\eta$ , the number of curves, and the minimum and maximum  $Re_r$  in each frame are as follows: (a) 35, 10, 21 and 71. (b) 70, 10, 71 and 247. (c) 139, 10, 260 and 595. (d) 279, 10, 823 and 1886. Curves A, B and C in each frame correspond to the three lowest values of  $Re_r$  (in ascending order). In (b) and (c), where inertial effects dominate (Fig. 5), the three labelled curves corresponding to the three lowest  $Re_r$  are distinct from the others (at higher  $Re_r$ ) which collapse. In frames (a) and (d) where non-inertial effects are more significant, the collapse of the unmarked curves is less pronounced. Dashed curve is the Gaussian distribution with zero mean and unity variance.

$(r\epsilon_r)^{1/3}$  is indeed close to zero in the inertial range. The correlation between  $V$  and  $(r\epsilon_r)^{1/3}$  in Fig. 9 is trivially zero due to homogeneity. At the largest scales, the non-zero correlation between  $V$  and  $(r\epsilon_r)^{1/3}$  may be due to the finite size of the domain.

The above results show that the stochastic variable  $V$  in the inertial range is independent of  $r$  and  $\epsilon_r$ , and that it is approximately universal. It then follows from Eq. 5 that the  $m$ -th order structure function in the iner-

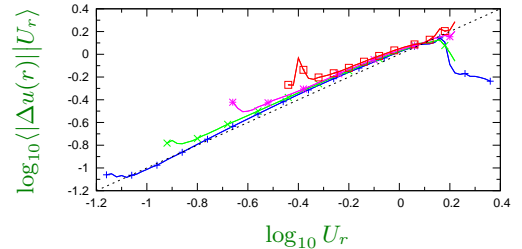


FIG. 8. (Color online) Logarithm of the mean of  $|\Delta u(r)|$  conditioned on the local velocity scale  $U_r = (r\epsilon_r)^{1/3}$  as a function of the logarithm of  $U_r$ . Symbols (+), (x), (\*), (□) correspond to inertial range separations  $r/\eta = 35, 70, 139$  and 279, respectively. Dashed line has a slope of 1.

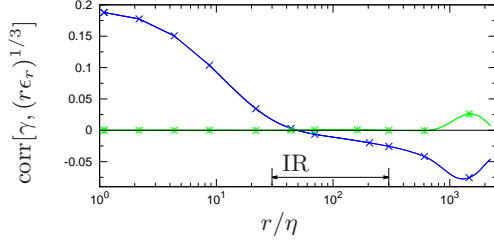


FIG. 9. (Color online) Correlation coefficient as a function of spatial separation between  $(r\epsilon_r)^{1/3}$  and the quantity  $\gamma$  where  $\gamma$  is either  $V(r)$  (\*) or  $|V(r)|$  (x), at  $R_\lambda \sim 650, 4096^3$ . The inertial range (IR) is marked for reference.

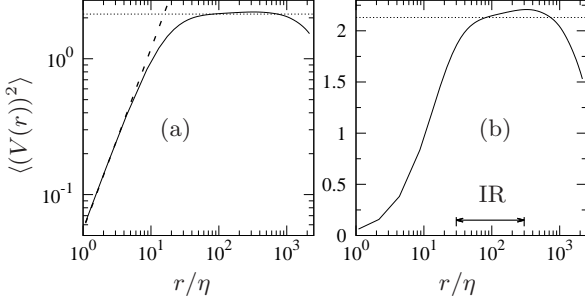


FIG. 10. Second moment of  $V$  at  $4096^3$ ,  $R_\lambda \sim 650$ . (a) Log-log scales to verify small- $r$  behavior, dashed line corresponds to  $r^{4/3}$  to check the small- $r$  slope. (b) Log-linear scales to check inertial range behavior; Dotted line at 2.13 for comparison with corresponding  $K41$  result. The inertial range (IR) extent from Fig. 5 is shown for reference.

tial range is given as

$$\langle [\Delta u(r)]^m \rangle = \langle V^m \rangle \langle (r\epsilon_r)^{(m/3)} \rangle. \quad (17)$$

In particular,  $\langle V(r) \rangle = 0$  in the inertial range. The second and third moments of  $V$  in the inertial range are related to the corresponding longitudinal velocity structure functions by

$$\langle (\Delta u(r))^2 \rangle = \langle V^2 \rangle \langle \epsilon_r^{2/3} \rangle r^{2/3}, \quad (18)$$

$$\langle (\Delta u(r))^3 \rangle = \langle V^3 \rangle \langle \epsilon_r \rangle r. \quad (19)$$

Figure 10 shows the second moment of  $V$  as a function of spatial separation. In the inertial range,  $\langle V^2 \rangle \approx 2.13$  (Fig. 10 (b)), which is comparable to the accepted estimates of the Kolmogorov constant in second-order structure functions (Refs. [4 and 19]). In the small- $r$  limit, a Taylor expansion shows that  $\langle V^2 \rangle$  varies as  $r^{4/3}$ , which is confirmed in Fig. 10 (a).

Comparing Eqs. 19 and 1, we see that  $\langle V^3 \rangle$  should be negative in the inertial range with a magnitude of  $4/5$ . Figure 11 shows the third moment of  $V$  (Eq. 19) at  $R_\lambda \sim 650$  as a function of spatial separation. In the inertial range,  $\langle V^3 \rangle = -0.8$  (Fig. 11 (b)), which is consistent with the exact  $K41$  result (Eq. 1). The quadratic form of  $\langle V^3 \rangle$  at  $r \approx \eta$  is confirmed in Fig. 11 (a) which shows a  $r^2$  behavior at the smallest scales.

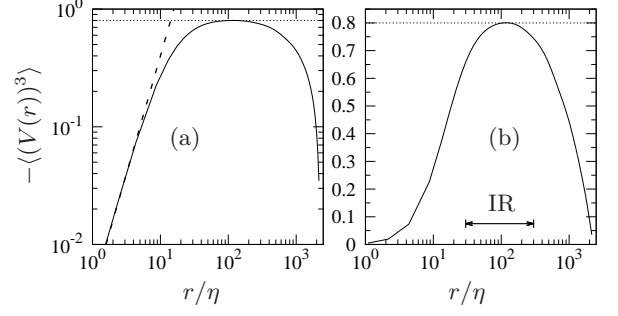


FIG. 11. Third moment of  $V$  at  $4096^3$ ,  $R_\lambda \sim 650$  (Eq. 19). (a) Log-log scales to check small- $r$  behavior, dashed line corresponds to  $r^2$  to check small- $r$  slope. (b) Log-linear scales to check inertial range behavior. Dotted line at 0.8 shows  $K41$  plateau. The inertial range (IR) extent from Fig. 5 is shown for reference.

The stochastic variable  $V$  is universal in the inertial range, in particular it is independent of  $r$  and  $\epsilon_r$  in this scale range. Hence it follows from Eq. 5 that  $\text{Var}(V^3) \langle r\epsilon_r \rangle^2 < \text{Var}(\Delta u(r)^3)$ , where  $\text{Var}(\cdot)$  denotes the variance of a random variable. Using homogeneity and dissipative anomaly [20], we get

$$\text{Var}(V^3) < \text{Var}\left(\frac{\Delta u(r)^3}{r\langle \epsilon \rangle}\right), \quad \text{for } \eta \ll r \ll L, \quad (20)$$

Even though  $V$  is the ratio of two intermittent quantities, it is well defined at least in the inertial range and that  $V$  is a better estimator of the  $K41$  constant than  $\Delta u(r)$ . This is consistent with Figs. 5 and 11 which show that  $\langle V^3 \rangle$  converges faster than  $\langle (\Delta u(r))^3 \rangle$  to the  $4/5$ th plateau.

#### D. K62: the first hypothesis

The statement of the first K62 postulate is that for  $r \ll L$ , the PDF of  $V$  depends only on  $Re_r$ . Since the viscosity is constant in our simulation, it is sufficient to check the dependence of  $V$  on  $r(r\epsilon_r)^{1/3}$ .

Figure 12 presents the PDF of  $V$  for two different spatial separations in the small scale regime. Different curves in each panel corresponds to different values of  $(r\epsilon_r)^{1/3}$ . The uncertainty in the data is appreciably higher than in the corresponding inertial range PDFs (Fig. 7), because the averaging intervals are smaller. Even so, the conclusion from Fig. 12 is that the PDF of  $V$  depends on  $(r\epsilon_r)^{1/3}$  and  $r$ .

As a further test, Fig. 13 shows the logarithm of the conditional mean of  $|\Delta u(r)|$ , conditioned on the local velocity as a function of the logarithm of the local velocity in the small  $r$  range. Evidently the curves for different spatial separations at the smallest scales do not collapse, confirming the dependence of  $V$  on  $(r\epsilon_r)^{1/3}$  and  $r$ .

In order to directly test the first hypothesis, Fig. 14 reports the conditional PDF of  $V$  for a fixed local Reynolds number ( $Re_r$ ). The PDFs in each frame correspond

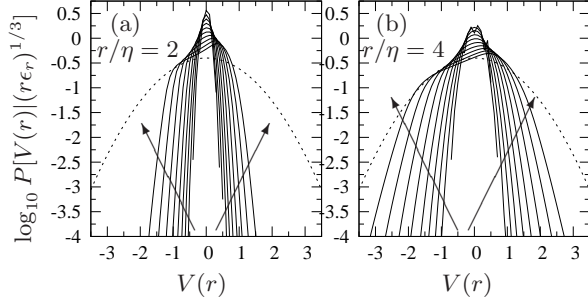


FIG. 12. Conditional PDF of  $V(r)$  in the small-scale range for a given spatial separation. The separation distance  $r$  (fixed for each frame), and the minimum and maximum values of  $Re_r$  are as follows: (a)  $r/\eta = 2$ ,  $Re_r$  ranging from 0.2 to 4.4. (b)  $r/\eta = 4$ ,  $Re_r$  ranging from 0.5 to 12.9. In each frame, there are 10 curves, each corresponding to a different  $Re_r$ , increasing in the direction shown. Dashed curve is the standard Gaussian distribution.

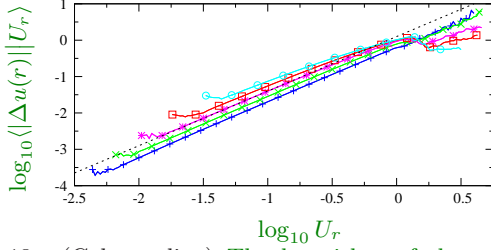


FIG. 13. (Color online) The logarithm of the expectation  $|\Delta u(r)|$  conditioned on the velocity scale  $U_r = (r\epsilon_r)^{1/3}$ , as a function of the logarithm of  $U_r$  for different spatial separations in the small  $r$  range. Symbols (+), ( $\times$ ), (\*), ( $\square$ ) and ( $\circ$ ) correspond to spatial separations  $r/\eta = 1, 2, 4, 8$  and  $16$ , respectively. Dashed line has slope of 1.5.

to different spatial separations ( $r$ ) and local velocities ( $(r\epsilon_r)^{1/3}$ ) such that the local Reynolds number  $Re_r$  is approximately the same. Since  $\epsilon_r$  is a random variable, exact correspondence in the values of  $Re_r$  is difficult, hence  $Re_r$  that are within 12% of each other are considered as approximately equal in this analysis. The PDFs collapse onto each other with some differences at the tails which can be attributed, at least in part to sampling uncertainties. From Fig. 14, it can be concluded that the PDF of  $V(r)$  only depends on the local Reynolds number  $Re_r$  for  $r \ll L$ .

In order to further test the dependence of  $V$  on the local Reynolds number in the small-scale range, consider the mean of  $r|\Delta u(r)|$ , conditioned on  $r(r\epsilon_r)^{1/3}$ ,

$$\langle r|\Delta u(r)||r(r\epsilon_r)^{1/3} \rangle = r(r\epsilon_r)^{1/3} \langle |V||r(r\epsilon_r)^{1/3} \rangle. \quad (21)$$

If  $V$  were only a function of  $Re_r$ , or  $r(r\epsilon_r)^{1/3}$  for  $r \ll L$ , then the above equation becomes

$$\langle r|\Delta u(r)||r(r\epsilon_r)^{1/3} \rangle = |V|r(r\epsilon_r)^{1/3}. \quad (22)$$

It follows that the left-hand-side of the Eq. 22 is only a function of  $r(r\epsilon_r)^{1/3}$  for  $r \ll L$ , if the first postulate is

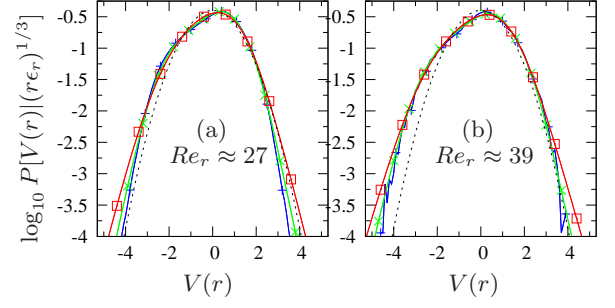


FIG. 14. (Color online) Conditional PDF of  $V(r)$  for a given local Reynolds number  $Re_r$ , for different spatial separations in the small-scale range. (a)  $Re_r \approx 27$  and (b)  $Re_r \approx 39$ . Symbols (+), ( $\times$ ), ( $\square$ ) correspond to spatial separations  $r/\eta = 4, 8$  and  $17$ , respectively. The exact values of  $Re_r$  are within 12% of each other in each panel. Dashed curve is the standard Gaussian distribution.

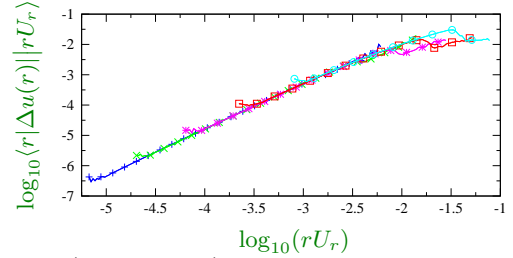


FIG. 15. (Color online) The logarithm of the expectation of  $r|\Delta u(r)|$  conditioned on  $rU_r$  ( $U_r = (r\epsilon_r)^{1/3}$ ), as a function of the logarithm of  $rU_r$  for different spatial separations in the small  $r$  range. Symbols (+), ( $\times$ ), (\*), ( $\square$ ) and ( $\circ$ ) correspond to spatial separations  $r/\eta = 1, 2, 4, 8$  and  $16$ , respectively.

valid. Figure 15 shows the logarithm of the left-hand-side of 22 plotted against the logarithm of  $r(r\epsilon_r)^{1/3}$  for different spatial separations in the small  $r$  range. The curves collapse on to one another except possibly at the tails where statistical uncertainty can be large, indicating that the first hypothesis is approximately valid at  $R_\lambda \sim 650$ .

The results corresponding to the small  $r$  regime presented here show support for the first refined similarity hypothesis. In contrast, previous work (Ref. [9]) on this topic has found evidence against the first similarity hypothesis. Subsequently the authors of Ref. [9] used an ad-hoc dependence on  $r$  and  $\epsilon_r$  to empirically determine the functional form of  $V$  at the smallest scales. We are of the opinion that the uncertainty in the PDF of  $V$  in Figs. 4(a) and 4(b) of Ref. [9] is at least partly a consequence of inadequate sampling. Effects of limited sampling are especially pronounced in the small  $r$  regime, because the averaging intervals are small. The problem of limited sampling is alleviated at least partly in our work by the use of 3D local averages of dissipation and the use of three different samples of  $V$  along the three orthogonal directions (Eq. 13). Consequently, there is less noise in the statistics of  $V$ , even when the averaging inter-



vals are small ( $r \sim \eta$ ). We have checked that decreasing the sample size by considering velocity increments  $\Delta u(r)$  only along one direction leads to considerable noise in the PDF of  $V$  at the smallest scales.

#### IV. CONCLUSIONS

We have compared and contrasted three-dimensional (3D) and one-dimensional (1D) local averages of dissipation. Since turbulence is three-dimensional, the 3D averaging is nominally the right procedure while 1D averaging has long been practiced as a matter of convenience. Further, the 3D averages of dissipation are influenced less by factors such as finite sampling and periodic boundary conditions than the 1D averaged dissipation. In particular, results from 3D averaging are less intermittent at the small scales than the 1D case, rendering the former more statistically stable than the latter.

Considering the advantages of 3D averaging, it seemed appropriate to use 3D averaged dissipation to examine the first and second postulates of K62 for a 4096<sup>3</sup> data set at  $R_\lambda \sim 650$ . The basic tenets of the first and second K62 postulates were found to be true. The variance and skewness of the variable  $V$  in the inertial range are shown to be consistent with the corresponding K62 predictions and  $V$  is approximately universal in this scale range. At the smallest scales, the statistics of  $V$  seem to depend only on the local Reynolds number to a good approximation.

In light of the support for the refined similarity hypotheses shown in this work, at least at the level of detail examined here, the following observations appear pertinent. For any singularity of exponent  $\alpha$  of  $r\epsilon_r$ , where  $\epsilon_r$  is the 3D local averaged dissipation and  $r \ll L$ , there exists an associated singularity of exponent  $h = \alpha/3$  for the velocity on the same set with fractal dimension  $D(h)$ ,

such that

$$h = \frac{\alpha}{3}, \quad D(h) = f(\alpha), \quad \zeta_p = \frac{p}{3} + \tau_{p/3}; \quad (23)$$

where  $f(\alpha)$  is the multifractal singularity spectrum [5, 21]. We are aware of objections of principle raised in [22] with regard to the refined similarity hypotheses and also of numerical results of [23] in which an alternative theory [24] seemed to agree marginally better with the simulations data. We point out that the previous work has not taken account of 3D averaging, which we advocate here as being more appropriate. It remains to be seen whether the refined similarity hypotheses stand when a more detailed assessment is attempted.

#### V. ACKNOWLEDGMENTS

We thank Rich Vuduc for his help with the computational aspects of this work. KI acknowledges funding from the European Research Council under the European Communitys Seventh Framework Program, ERC Grant Agreement No 339032. This work is partially supported by the National Science Foundation (NSF), via Grants CBET-1139037, OCI-0749223 and OCI-1036170 at the Georgia Institute of Technology. The computations were performed using supercomputing resources provided through the XSEDE consortium (which is funded by NSF) at the National Institute of Computational Sciences at the University of Tennessee (Knoxville), the Texas Advanced Computing Center at the University of Texas (Austin), and the Blue Waters Project at the National Center for Supercomputing Applications at the University of Illinois (Urbana-Champaign).

- 
- [1] A. N. Kolmogorov, Dokl. Akad. Nauk. SSSR **30**, 299 (1941a).
  - [2] A. N. Kolmogorov, Dokl. Akad. Nauk. SSSR **434**, 16 (1941b).
  - [3] P. K. Yeung, D. A. Donzis, and K. R. Sreenivasan, J. Fluid Mech. **700**, 5 (2012).
  - [4] A. S. Monin and A. M. Yaglom, *Statistical Fluid Mechanics*, Vol. 2 (MIT Press, 1975).
  - [5] U. Frisch, *Turbulence* (Cambridge University Press, 1995).
  - [6] K. R. Sreenivasan and R. A. Antonia, Annu. Rev. Fluid Mech. **29**, 435 (1997).
  - [7] A. N. Kolmogorov, J. Fluid Mech. **13**, 82 (1962).
  - [8] A. M. Obukhov, J. Fluid Mech. **13**, 77 (1962).
  - [9] G. Stolovitzky, P. Kailasnath, and K. R. Sreenivasan, Phys. Rev. Lett. **69**, 1178 (1992).
  - [10] Huang Y. and Schmitt F. G., J. Fluid Mech. **741**, R2 (2014).
  - [11] L. P. Wang, S. Chen, J. G. Brasseur, and J. C. Wynngaard, J. Fluid Mech. **309**, 113 (1996).
  - [12] V. Eswaran and S. B. Pope, Comput. Fluids **16**, 257 (1988).
  - [13] R. S. Rogallo, NASA Tech. Memo 81315, NASA Ames Research Center (1981).
  - [14] D. A. Donzis, P. K. Yeung, and D. Pekurovsky, in *Proc. TeraGrid '08 Conf.* (2008).
  - [15] K. P. Iyer, *Studies of turbulence structure and turbulent mixing using Petascale computing*, Ph.D. thesis, Georgia Institute of Technology (2014).
  - [16] Hinkley D. V., Biometrika **56**, 635 (1969).
  - [17] K. R. Sreenivasan, R. A. Antonia, and H. Q. Danh, Phys. Fluids **20**, 1238 (1977).
  - [18] K. R. Sreenivasan, Phys. Fluids **7**, 2778 (1995).
  - [19] P. K. Yeung and Y. Zhou, Phys. Rev. E **56**, 1746 (1997).
  - [20] K. R. Sreenivasan, Phys. Fluids **10**, 528 (1998).
  - [21] Meneveau, C. and Sreenivasan, K. R., J. Fluid Mech. , 429 (1991).
  - [22] U. Frisch, Proc. R. Soc. Lond. A **434**, 89 (1991).
  - [23] J. Schumacher, K. R. Sreenivasan, and V. Yakhot, New J. Phys. **9**, 89 (2007).

- [24] V. Yakhot, Phys. Rev. E **63**, 026307 (2001).